# X-ray–$\gamma$ fast-timing lifetime measurement of the $6_1^+$ state in $^{206}$Po

K. Stoychev ●,[1,2,*] M. Djongolov,[1] V. Karayonchev,[1,3] G. Rainovski,[1] M. Ley,[3] J. Jolie,[3] D. Bittner,[3] A. Blazhev,[3] F. Dunkel,[3]
A. Esmaylzadeh ●,[3] C. Fransen,[3] J. Garbe,[3] L. M. Gerhard,[3] R.-B. Gerst,[3] K. Geusen,[3] K. A. Gladnishki,[1] G. Häfner,[2,3]
D. Kalaydjieva ●,[1] L. Klöckner,[3] L. Knafla,[3] D. Kocheva,[1] L. Kornwebel,[3] C. Müller-Gatermann,[3,†]
E. Nikodem,[3] J.-M. Régis,[3] K. Schomacker,[3] and M. Stoyanova ●[1]

[1]*Faculty of Physics, Saint Kliment Ohridski University of Sofia, 1164 Sofia, Bulgaria*
[2]*Université Paris-Saclay, Centre National de la Recherche Scientifique, IN2P3, IJCLab, 91405 Orsay, France*
[3]*Institut für Kernphysik, Universität zu Köln, 50937 Köln, Germany*

Low-lying states in $^{206}$Po were investigated using the fast-timing technique with LaBr$_3$(Ce) and high-purity germanium detectors. The excited states in this nucleus were populated via two consecutive electron capture decays from $^{206}$Rn. The parent isotope was produced in the $^{194}$Pt($^{16}$O, $4n$)$^{206}$Rn fusion-evaporation reaction at the FN-Tandem facility at the Institute for Nuclear Physics, University of Cologne. The previously known value for the lifetime of the $4_1^+$ state in $^{206}$Po was confirmed using the generalized centroid difference (GCD) method. The lifetime of the $6_1^+$ state was determined from $\beta$ decay in the first application of the GCD method for x-ray–$\gamma$ coincidences. A Monte Carlo based approach was applied to address the indirect population of the $6_1^+$ state by the decay of $^{206}$At. The experimental results were examined in the context of the transition of single-particle excitations to collective behavior in the neutron-deficient Po isotopes. The obtained $B(E2; 6_1^+ \to 4_1^+)$ value suggests that for the $6_1^+$ states in even-even Po isotopes the transition from a noncollective regime at $N = 126$ to a collective regime occurs at $N \leqslant 120$.

## I. INTRODUCTION

One of the fundamental features of atomic nuclei is their shell structure characterized by the magic numbers, the emergence of which is naturally explained within the nuclear shell model with the introduction of the spin-orbit interaction [1]. In particular, the low-energy spectra of semimagic nuclei are interpreted in the same framework via the addition of pairing correlations. In semimagic nuclei with multiple particles in a high-$j$ orbital, the low-energy $J > 0$ excited states are formed by recoupling of the angular momenta of the unpaired nucleons. The resulting multiplets of states can be classified by a quantum number—seniority ($\nu$) [2–4], which is the number of the unpaired nucleons. It is considered to be a good quantum number when $j$ of the involved orbitals is high, e.g., the region above $^{208}$Pb where the $\nu(g_{9/2})$ and the $\pi(h_{9/2})$ orbitals play a major role in the forming of the low-energy states. In these cases the generalized seniority scheme, which also accounts for degenerate levels, is used to truncate the shell model space in theoretical calculations [3,4].

For the yrast states in even-even nuclei there are several clear experimental signatures emerging from the seniority scheme [5,6]. The energy difference between the excited states with seniority $\nu = 2$ decreases towards the state with the highest angular momentum. Also, the absolute $E2$ transition strength has a parabolic dependence on the filling of the $j$ shell for both seniority-conserving ($\Delta\nu = 0$) transitions $J \to J - 2$ ($J \geqslant 4$) and the seniority-changing ($\Delta\nu = 2$) transition $2_1^+ (\nu = 2) \to 0_{\mathrm{GS}}^+ (\nu = 0)$, with a minimum and a maximum at the middle of the $j$ shell, respectively [4]. These features are expected to persist in open-shell nuclei close to magic numbers if the low-energy multiplet is constructed mainly by nucleons of the same kind ($p$ or $n$). However, adding valence nucleons of the other kind leads to an increase of the proton-neutron interaction and, consequently, to breaking down of the pairing correlations [7] and thus to an emergence of collective behavior. The latter can be deemed as a transition from seniority-type single-particle excitations to collective excitations. This transition could be the result of a breaking down of the corresponding seniority symmetry due to cross-shell core excitations, as shown recently by Mach *et al.* [8].

A suitable region for studying this transition is the Po-Rn-Ra region in the vicinity of the doubly magic nucleus $^{208}$Pb. The protons in the $h_{9/2}$ orbital interact weakly with the valence neutrons in nuclei with $N \leqslant 126$ [9] due to the high principal quantum number and low angular momentum of the relevant neutron orbitals [5]. As a result, the $\pi(h_{9/2})^n$ configuration is dominant in the wave functions of the yrast states that consequently exhibit a seniority-type structure. Indeed, in even-even Po-Rn-Ra nuclei with $122 \leqslant N \leqslant 126$ the $8_1^+$ states are isomers and the measured constant values of their magnetic moments [10] support the notion of prevalence of

*Corresponding author: konstantin.stoychev@ijclab.in2p3.fr
†Present address: Argonne National Laboratory, 9700 South Cass Avenue, Lemont, Illinois 60439, USA.

the $\pi(h_{9/2})^n$ configuration in the wave functions [11]. Additionally, the even-even Po-Rn-Ra nuclei in the $120 \leqslant N \leqslant 126$ isotonic chains exhibit a decrease in the reduced transition probability $B(E2; 8_1^+ \rightarrow 6_1^+)$ values with the filling of the proton $h_{9/2}$ orbital. These experimental signatures have lead Ressler *et al.* [5] to suggest that the seniority regime persists for Po-Rn-Ra nuclei in the $122 \leqslant N \leqslant 126$ chains up to $^{206-210}$Ra and collective behavior becomes prevalent around $N = 118$–120.

However, recent experimental results and calculations [12] indicate that in Po isotopes the transition from single-particle seniority-type excitations to collective excitations has a pronounced spin-dependent behavior. Specifically, reported measurements of $B(E2; 2_1^+ \rightarrow 0_{GS}^+)$ values for $^{206}$Po and $^{208}$Rn suggest that for the $2_1^+$ states in Po isotopes collectivity emerges readily with moving away from the closed proton shell [12]. In addition, the $B(E2; 4_1^+ \rightarrow 2_1^+)$ values from a recent study by Stoyanova *et al.* [13] indicate that collective behavior of the $4_1^+$ states in Po isotopes develops below $N = 124$. The known $B(E2; 6_1^+ \rightarrow 4_1^+)$ value for $^{208}$Po [14] suggests that seniority of the $6_1^+$ state is still conserved at $N = 124$. In order to determine whether the collectivity of the $6_1^+$ states in Po isotopes becomes prevalent at or below $N = 122$, a measurement of the lifetime of the $6_1^+$ state in $^{206}$Po has been carried out. This paper is a continuation of the current collaboration's study of seniority in the Po-Rn-Ra region, which includes the work of Stoyanova *et al.* [13].

## II. EXPERIMENT

The experiment was performed at the HORUS spectrometer [15] of the FN-Tandem facility of the Institute for Nuclear Physics at the University of Cologne. An $^{16}$O beam at an energy of 84 MeV was used to induce the $^{194}$Pt($^{16}$O, $4n$)$^{206}$Rn fusion-evaporation reaction on a 4 mg/cm$^2$ $^{194}$Pt target. In addition, a foil of 180 mg/cm$^2$ bismuth was used to stop the beam, together with a 140 mg/cm$^2$ copper layer for heat dissipation. The $^{206}$Po nuclei were populated via two successive electron capture (EC) decays from the initial $^{206}$Rn [$T_{1/2} = 5.67(17)$ min; $\varepsilon = 38\%$] and its daughter nucleus $^{206}$At [$T_{1/2} = 30.6(8)$ min; $\varepsilon = 99.1\%$].

A hybrid detector array consisting of eight coaxial high-purity germanium (HPGe) detectors and 11 lanthanum bromide (LaBr) detectors was used for $\gamma$-ray detection. Bismuth germanate oxide (BGO) scintillators were used as active Compton scattering shields for six of the LaBr detectors with cylindrical $1.5 \times 1.5$ in. crystals. The rest of the LaBr detectors with conical $1 \times 1.5 \times 1.5$ in. crystals had passive Pb shields for suppression of the scattered-$\gamma$-ray background.

The time differences from every unique pair of LaBr detectors were acquired using time-to-amplitude converters (TACs) set up in the multiplexed-start and multiplexed-stop electronics configuration [16]. The experiment was run in triggerless mode in which the detector energy signals and TAC output signals were recorded in a listmode format. The full set of in-beam data ($\approx 100$ h) was used in the analysis as well as $\approx 5$ h of off-beam data.

## III. ANALYSIS

The goal of the experiment is to measure the unknown lifetime of the $6_1^+$ state in $^{206}$Po which we expect to be in the range of hundreds of picoseconds based on the systematics of the known lifetimes of the state in $^{208,210}$Po [14,17]. Furthermore, the $4_1^+$ state in $^{206}$Po would also be accessible which provides a good opportunity for its lifetime confirmation under the current experimental conditions. Both lifetimes of interest can be extracted via the generalized centroid difference (GCD) method [18], briefly outlined below.

The GCD method uses two independent distributions (delayed and antidelayed) of the time difference $\Delta T$ between two consecutive $\gamma$ rays the populating (feeder) and depopulating (decay) transitions of the level of interest. The delayed (D) distribution is obtained when the feeder transition provides the start signal to a TAC and the decay transition provides the corresponding stop signal. In the opposite case, the resulting $\Delta T$ distribution is denoted as antidelayed (AD). The mean lifetime of the level of interest can be obtained from the difference of the centers of mass of these distributions, $C_D$ and $C_{AD}$, respectively, via the relation

$$\Delta C \equiv C_D - C_{AD} \equiv 2\tau + \text{PRD}. \quad (1)$$

Here PRD is the prompt response difference (PRD) function that characterizes the mean energy dependence of the time walk of the fast-timing setup [19]. Obtaining the PRD curve for the particular setup is essential for the application of the GCD method and is accomplished using $^{152}$Eu and $^{133}$Ba calibration source data, covering the energy range between 40 and 1408 keV. The delayed and antidelayed time-difference spectra are obtained for several feeder-decay transitions for states with known lifetimes. The resulting centroid differences used together with Eq. (1) yield the corresponding PRD values. These data points are then fitted with the function [21]

$$\text{PRD}(E_\gamma) = \frac{a}{\sqrt{E_\gamma + b}} + cE_\gamma^2 + dE_\gamma + e, \quad (2)$$

as shown in Fig. 1. The uncertainty contribution to the lifetime measurement from the PRD is taken as two times the root mean square from the fit ($2\sigma$).

The data are sorted into triple HPGe-LaBr-LaBr coincidences where a gate on the HPGe detectors is used to select the cascade of interest. Additionally, triple HPGe-HPGe-LaBr coincidences are used to check for presence of contaminating transitions in the doubly gated LaBr spectra relevant for the time measurements. The higher-energy resolution of the HPGe detectors allows us to discern low-intensity transitions which are difficult to identify in LaBr energy spectra. A comparison between the full projections obtained from the two types of coincidences is shown in Fig. 2. A partial level scheme of the levels of interest in $^{206}$Po is shown in Fig. 3.

To extract the lifetime of the $4_1^+$ state, a HPGe energy gate is set on the $2_1^+ \rightarrow 0_{GS}^+$ transition and LaBr energy gates are set on the $6_1^+ \rightarrow 4_1^+$ and $4_1^+ \rightarrow 2_1^+$ transitions. An additional TAC coincidence window $|\Delta T| \leqslant 2$ ns is used when the final LaBr-TAC matrices are produced in order to lower the background contribution from random coincidences in the doubly gated
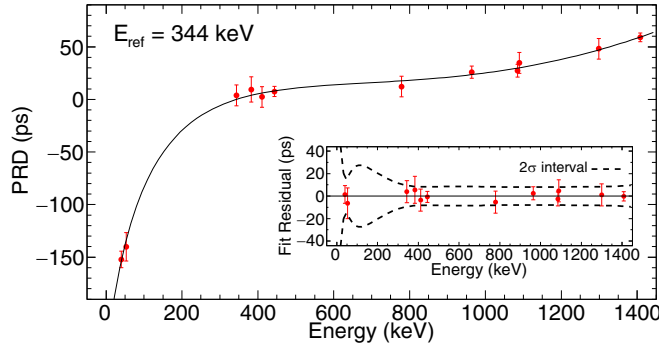
FIG. 1. The PRD curve of the setup. The data points have been obtained from [152]Eu and [133]Ba calibration sources. The 344 keV transition in [152]Eu is used as a reference energy [19]. The deviation of each point from the curve is shown in the inset, as well as the $2\sigma$ interval calculated analytically from the covariance matrix of the fit, following the procedure in [20]. The increased uncertainty in the 60–300 keV region stems from the lack of suitable calibration points to determine the exact behavior of the PRD curve.

LaBr projections. The resulting time-difference spectra along with the relevant doubly gated LaBr and HPGe projections are shown in Fig. 4. The centroid difference of the delayed and antidelayed time distributions is determined to be $\Delta C_{\mathrm{exp}} = 178(10)$ ps. This value cannot be used directly in Eq. (1) as it contains contributions from the time-correlated background underneath the full-energy peaks (FEPs). In Fig. 4(a) several regions around the FEP of the feeding transition are selected and the corresponding centroid differences of the background are obtained. The resulting data points are fitted with a linear function to interpolate the centroid difference of the background $\Delta C_f^{\mathrm{BG}}$ underneath the FEP of the feeding transition $E_f$ [23]. Following a similar procedure $\Delta C_d^{\mathrm{BG}}$ is determined [see Figs. 4(d) and 4(e)]. The background-corrected centroid difference $\Delta C_{\mathrm{FEP}}$ is defined by [24]

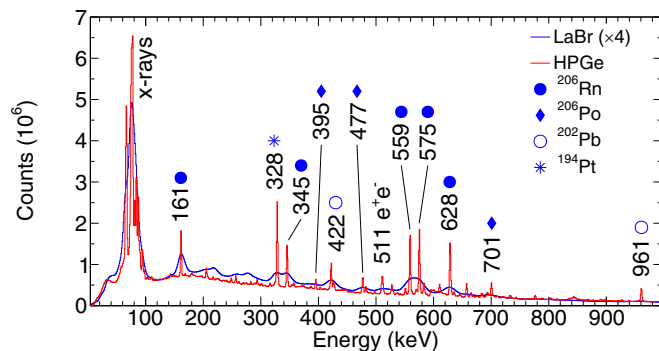$$\Delta C_{\mathrm{FEP}} \equiv \Delta C_{\mathrm{exp}} + \tilde{t}_{\mathrm{cor}}, \qquad (3)$$



FIG. 2. Full projections obtained from HPGe-LaBr-LaBr (blue) and HPGe-HPGe-LaBr (red) coincidences. Denoted are transitions from the reaction product [206]Rn, the even-even decay products [206]Po and [202]Pb, and the Coulomb excitation of the target [194]Pt.
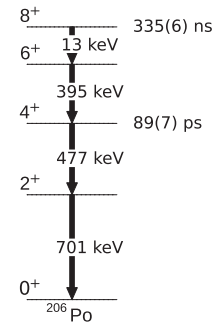


FIG. 3. Partial level scheme of [206]Po with the known mean lifetimes of the $4_1^+$ and $8_1^+$ states, taken from Refs. [13] and [22], respectively. The plot of the $8_1^+ \to 6_1^+$ transition is exaggerated for clarity.

where

$$\tilde{t}_{\mathrm{cor}} \equiv \frac{t_{\mathrm{cor}}(E_d)(p/b)_f + t_{\mathrm{cor}}(E_f)(p/b)_d}{(p/b)_f + (p/b)_d}, \qquad (4)$$

$$t_{\mathrm{cor}}(E_{f,d}) \equiv \frac{\Delta C_{\mathrm{exp}} - \Delta C_{f,d}^{\mathrm{BG}}}{(p/b)_{f,d}}. \qquad (5)$$

The centroid difference $\Delta C_{\mathrm{FEP}}$ is calculated to be 197(18) ps and Eq. (1) becomes [16]

$$\Delta C_{\mathrm{FEP}} = 2\tau + \mathrm{PRD}. \qquad (6)$$

The final result for the lifetime of the $4_1^+$ state in [206]Po is determined to be $\tau(4_1^+) = 101(8)$ ps which is in agreement with the reported value of 89(7) ps from Ref. [13], within uncertainties. The corresponding $B(E2; 4_1^+ \to 2_1^+)$ values are $316_{-21}^{+27}$ $e^2$ fm$^4$ (4.4$_{-0.4}^{+0.5}$ W.u.) and 359(28) $e^2$ fm$^4$ [5.0(4) W.u.] [13], respectively.

The GCD method was additionally applied to measuring the well-known lifetime of the $2_1^+$ state in [194]Pt. The HPGe gate was set on the 562 keV $(5_1^-) \to 4_1^+$ transition and the LaBr gates were set on the 483 keV $4_1^+ \to 2_1^+$ and 328 keV $2_1^+ \to 0_{\mathrm{GS}}^+$ transitions. The extracted lifetime for the $2_1^+$ state in [194]Pt is 59(7) ps, which is in good agreement with the adopted value of 60.2(25) ps [25]. This serves as validation of the obtained value of $\tau(4_1^+)$ in [206]Po as well as for applying the GCD method to extract the lifetime of the $6_1^+$ state, the measurement of which proved to be challenging due to the following factors.

The yrast feeding transition $8_1^+ \to 6_1^+$ has an energy of 12.5 keV and thus is not registered by the $\gamma$-ray detectors, while the known off-yrast feeding transitions are not sufficiently populated to be of use in a fast-timing analysis. A possibility to circumvent this obstacle is to use the Po x rays emitted from the EC decay of [206]At $\to$ [206]Po, as shown to be a viable approach in Ref. [24]. Around 38% [26] of the decays of [206]At (considering only EC decays that constitute 99.1% of all [206]At decays [22]) directly populate the $6_1^+$ state in [206]Po which would make the application of the GCD method possible by using the emitted Po x rays as a start signal and the $6_1^+ \to 4_1^+$ transition as a stop signal. However, 41% of the decays of [206]At populate excited states above the $6_1^+$ state [26] and could reach that state through intermediate $\gamma$ transitions,
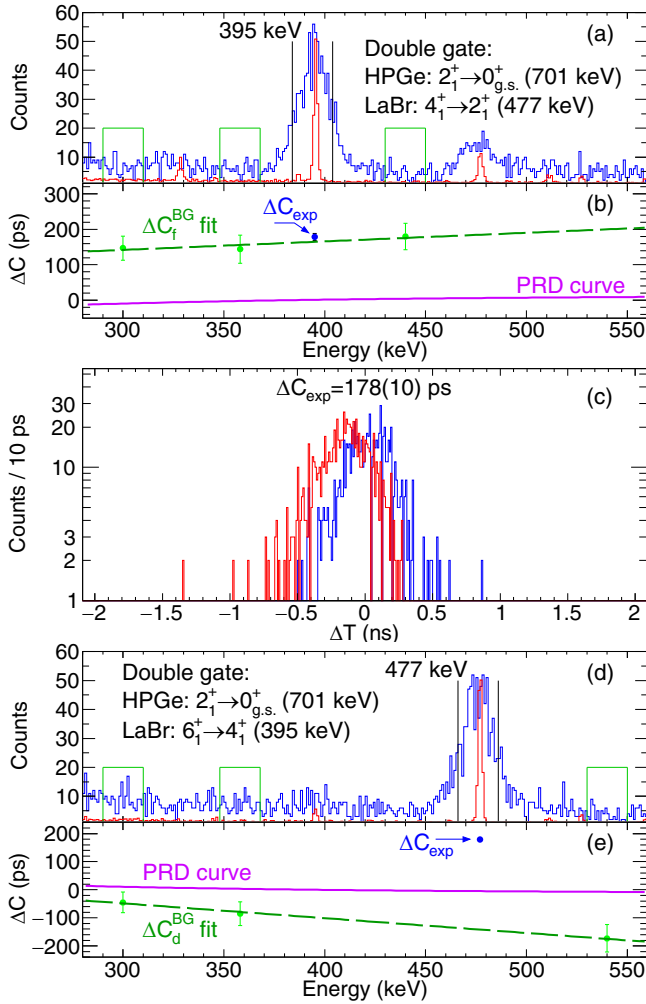
FIG. 4. (a) LaBr (blue) and HPGe (red) detector projections, produced after applying double HPGe-LaBr gates on the HPGe-LaBr-LaBr and HPGe-HPGe-LaBr coincidences, respectively. The LaBr gate is set on the decay transition. The HPGe spectrum is scaled by a factor of 0.047. The vertical black lines indicate the LaBr gate width on the feeding transition used to produce the time-difference spectra. The corresponding peak to background ratio for the feeding transition is $(p/b)_f = 7.0(1)$. The regions marked in green denote the gates used to extract the centroid difference of the background (see text). (b) The linear fit of the background centroid difference underneath the full-energy peak of the feeding transition (dashed green line), the PRD curve of the setup (violet line), and the experimentally obtained centroid difference (blue point). (c) The delayed (blue) and antidelayed (red) time-difference spectra for the 395–477 keV feeder-decay transitions used for extracting the lifetime of the $4_1^+$ state. (d) Analogous to (a) with the LaBr gate set on the feeding transition. The HPGe spectrum is scaled by a factor of 0.055. The corresponding peak to background ratio is $(p/b)_d = 8.2(14)$. (e) Analogous to (b).

all of which would contribute to the time-difference spectra via their corresponding lifetimes. This nondirect feeding to the $6_1^+$ state is taken into consideration in the analysis.

For the extraction of the lifetime of the $6_1^+$ state the HPGe gate is set on the $2_1^+ \rightarrow 0_{GS}^+$ transition as this gate proved to

yield a better background suppression in the doubly gated LaBr spectra compared to one placed on the $4_1^+ \rightarrow 2_1^+$ transition. The same TAC coincidence window $|\Delta T| \leqslant 2$ ns is used to further reduce random coincidences and improve the peak to background ratio in the doubly gated spectra. The two LaBr gates are set on the x-ray region and the $6_1^+ \rightarrow 4_1^+$ transition. The resulting doubly gated energy spectra and time-difference spectra for the $6_1^+$ state are presented in Fig. 5. Taking into account the background correction, a value of $\Delta C_{FEP} = 518(46)$ ps is obtained, for which Eq. (6) produces $\tau_{exp} = 313(23)$ ps. It has to be stressed that this value contains the true lifetime of the $6_1^+$ state as well as contributions from the lifetimes of states above the $6_1^+$ state. This value can be mathematically modeled as

$$
\begin{aligned}
\tau_{exp} &= f\tau(6_1^+) + (1-f)[\tau(6_1^+) + \tau_{side}] - \Delta t_p \\
&= \tau(6_1^+) + (1-f)\tau_{side} - \Delta t_p, \quad (7)
\end{aligned}
$$

where $f$ is the fraction of the decays of $^{206}$At that directly populate the $6_1^+$ state in $^{206}$Po and $\tau_{side}$ is an effective lifetime from all intermediate states above the $6_1^+$ state, as shown in Fig. 6. The term $\Delta t_p$ in Eq. (7) is a correction due to the applied TAC coincidence window. This correction is necessary as the upper limit of the $|\Delta T| \leqslant 2$ ns window acts as a partitioning point $T_p^D$ that separates the delayed time-difference distribution in two regions. Due to the exponential tail of the distribution there is a nonzero probability for counts to occur beyond $T_p^D = 2$ ns. These counts are consequently not included in the determination of the experimental centroid $C_D$ of the delayed distribution. The case of the antidelayed distribution is analogous for $C_{AD}$, with a partitioning point at $T_p^{AD} = -2$ ns. Since $\tau_{exp}$ is derived from both spectra within the coincidence window, the effect from partitioning of the distributions results in a deviation of $\tau_{exp}$ from the true weighted sum of lifetimes. A short description of the properties of a distribution partitioned in two regions, including the structure of the $\Delta t_p$ term, is given in the Appendix. The value of $\Delta t_p$ is experimentally inaccessible and thus several new observables that arise from such partitioning are utilized in the analysis instead, as described further below. Additionally, an unambiguous extraction of the $6_1^+$ lifetime using the model Eq. (7) would require knowing both the fraction of direct feeding $f$ and $\tau_{side}$. The value of $f$ can be estimated from the experimental data, while only an upper and lower limit can be set for the value of $\tau_{side}$, subject to certain experimental constraints.

The value of the fraction of direct feeding $f$ is determined from triple HPGe-HPGe-HPGe coincidence data. A random-background-subtracted HPGe-gated $\gamma$-$\gamma$ matrix is sorted for which the HPGe gate is set on the $2_1^+ \rightarrow 0_{GS}^+$ transition (701 keV). An additional HPGe-gated $\gamma$-$\gamma$ matrix is prepared with HPGe gates set on the background close to the 701 keV line. This background matrix is subtracted from the original HPGe-gated matrix to reduce the contribution of the Compton background underneath the 701 keV line. Applying a cut on the $6_1^+ \rightarrow 4_1^+$ transition (395 keV) in the resultant background-subtracted matrix produces the projection shown in Fig. 7. Efficiency calibration for the HPGe detectors has been carried out using the $^{152}$Eu source data to allow for a comparison to be made between the intensities of different
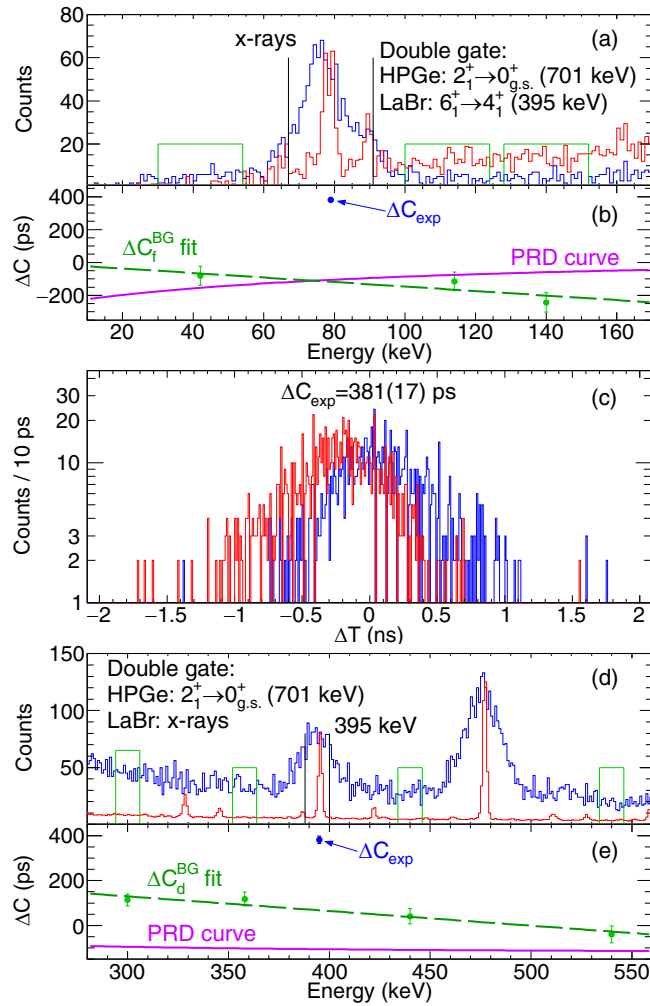
FIG. 5. The figure is analogous to Fig. 4. (a) The LaBr gate on the x-ray region (vertical black lines) is not set on the full width of the x-ray peak in order to increase the peak to background ratio. The three peaks observed in the HPGe spectrum are the $^{194}$Pt $K_\alpha$ and the $^{206}$Po $K_\alpha$ and $K_\beta$ x rays. The contribution of the $^{194}$Pt $K_\alpha$ to the time-difference spectra is via random coincidences and is accounted for by the background-correction procedure. The HPGe spectrum is scaled by a factor of 0.5. The corresponding peak to background ratio is $(p/b)_f = 7.9(7)$. (b) The linear fit of the background centroid difference (dashed green line), the PRD curve of the setup (violet line), and the experimentally obtained centroid difference (blue point). (c) The delayed (blue) and antidelayed (red) time-difference spectra for the (x-ray) 395 keV feeder-decay transitions used for extracting the lifetime of the $6_1^+$ state. (d) The LaBr gate on the decay transition is narrower compared to the LaBr gate used in the extraction of the lifetime of the $4_1^+$ state [Fig. 4(a)] in order to increase the peak to background ratio, which is $(p/b)_d = 2.0(5)$. The HPGe spectrum is scaled by a factor of 0.02. (e) Analogous to (b).

lines in the matrix projection. The direct feeding fraction can be measured through the ratio of the intensities of the nonyrast feeding transitions of the $6_1^+$ state and the intensity of the $4_1^+ \rightarrow 2_1^+$ transition which is equal to the full intensity of the $6_1^+ \rightarrow 4_1^+$ transition due to the applied cut on 395 keV. We consider the two observed known nonyrast feeding transitions as
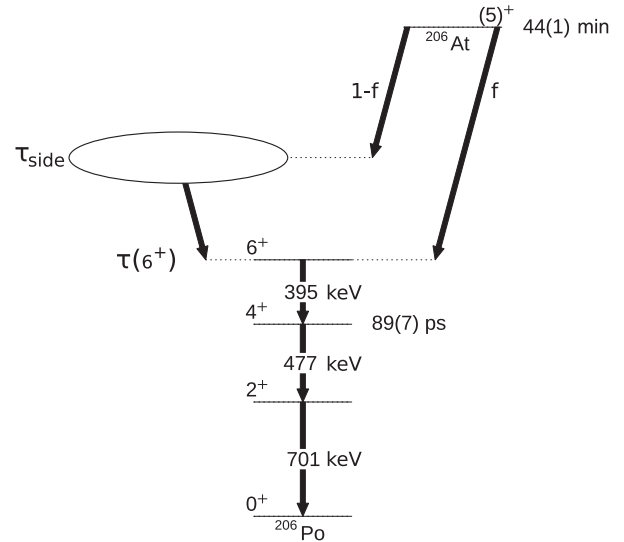
FIG. 6. Schematic representation of the contributions to the experimentally determined lifetime of the $6_1^+$ state. The EC of $^{206}$At populates the $6_1^+$ either directly or through one or more intermediate excited states in $^{206}$Po (denoted as an ellipse) characterized with an effective lifetime $\tau_{\text{side}}$. Note that the contribution from the long mean lifetime of the $8_1^+$ state [335(6) ns] is absorbed in $\tau_{\text{side}}$ but is highly suppressed due to the applied 2 ns TAC coincidence window (see text).

well as all observed lines in Fig. 7, which are not placed in the adopted level scheme, as being direct feeding transitions of the $6_1^+$ state. The efficiency-corrected intensities of the assumed
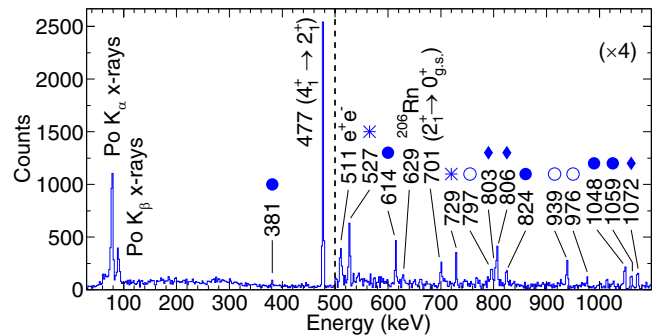
FIG. 7. The doubly gated HPGe projection from triple HPGe-HPGe-HPGe coincidences with the gates set on the $2_1^+ \rightarrow 0_{GS}^+$ (701 keV) and $6_1^+ \rightarrow 4_1^+$ (395 keV) transitions. The histogram is presented with 2 keV per bin and the bins in the spectrum above 500 keV are scaled by a factor of 4 for better visibility. Denoted are the known transitions directly populating the $6_1^+$ state (star); transitions known from the level scheme of $^{206}$Po (filled circle); transitions known to be from $^{206}$Po that are not placed on the level scheme (empty circle); and newly observed transitions (diamonds) that are assumed to be from $^{206}$Po due to the double HPGe coincidence conditions imposed. Note that there are two known transitions with an energy close to 806 keV in the level scheme of $^{206}$Po (805.9 keV $11_2^- \rightarrow 9_1^-$ and 806.6 keV $13_1^- \rightarrow 11_1^-$). The observed line at 806.5 keV is therefore considered a new transition as both the current experimental data and Ref. [26] show that the $11_2^-$ and $13_1^-$ states are not populated in the EC of $^{206}$At, which has a ground-state spin 5.

TABLE I. The experimentally determined energy and efficiency-corrected intensity of the assumed direct feeding transitions in the doubly gated HPGe energy spectrum (see Fig. 7), compared to the known literature values taken from Ref. [26]. The intensity is given relative to that of the 477 keV transition, depopulating the $4_1^+$ state.

| $E_{\mathrm{exp}}$ (keV) | $E_{\mathrm{lit}}$ (keV) | $I_\gamma$ |
|---|---|---|
| 476.99(2) | 477.10(3) | 100 |
| 527.21(8) | 527.27(7) | 7.1(6) |
| 729.15(15) | 729.27(15) | 4.3(5) |
| 796.01(16) | 796.60(11) | 3.2(6) |
| 802.48(29) | 802.50(15) | 2.3(5) |
| 806.33(12) | | 6.6(7) |
| 938.92(19) | 939.25(7) | 5.4(7) |
| 976.13(24) | 976.32(10) | 1.1(3) |
| 1072.18(20) | 1071.78(19) | 3.3(6) |

direct feeding transitions of the $6_1^+$ state are presented in Table I. From these intensities a direct feeding fraction of $f = 0.67(2)$ is obtained.

In general, this value is also affected by the pandemonium effect [27], which would lower the value of $f$ with respect to the measured one via unobserved intensities of high-energy $\gamma$ transitions feeding the state of interest. Unfortunately, due to the nature of the pandemonium effect, any such unobserved transitions would be indistinguishable from the direct feeding of the $6_1^+$ state using solely spectroscopic data. Still, the highest-lying state populated in the decay of $^{206}$At at 4.7 MeV is relatively close to the $Q$ value of the decay $Q_\beta = 5.4$ MeV and, in addition, $\gamma$ transitions up to 2.7 MeV have been identified in the original study of the $^{206}$At decay [26]. These empirical observations can serve as an indication that the pandemonium effect would not be very pronounced in $^{206}$Po and would not impact the current analysis and the obtained direct feeding fraction $f$ significantly.

The other unknown parameter in Eq. (7) is the effective lifetime $\tau_{\mathrm{side}}$ of the intermediate excited states above the $6_1^+$ state. This lifetime cannot be determined experimentally and thus we will investigate its influence on the range of values of $\tau(6_1^+)$ for which Eq. (7) remains valid within the experimental uncertainty of $\tau_{\mathrm{exp}}$. Following this approach an upper and lower limit for $\tau(6_1^+)$ can be determined, and the center of that interval will be assigned as the final value of $\tau(6_1^+)$.

To obtain the lower limit for the $6_1^+$ lifetime, a Monte Carlo simulation of the delayed time-difference spectrum is utilized, taking into account the assumed feeding model of the $6_1^+$ state. The free parameters of the simulation are two separate $B(E2)$ values—one is assigned to the $6_1^+ \rightarrow 4_1^+$ transition, and the other one is simultaneously assigned to all the transitions feeding the $6_1^+$ state, which also are assumed to be of pure E2 character. The simulated time-difference spectrum uses the individual intensities of the feeders, given in Table I, as they govern the probabilities with which the different decay paths are taken in the simulation process. A fine grid of $B(E2)$ values is considered—from 3 to 8 W.u. in steps of 0.01 W.u. for the $B(E2, 6_1^+ \rightarrow 4_1^+)$ and from 0.001 to 1 W.u. in steps of 0.002 W.u. for all feeders of the $6_1^+$ state. For every pair of

$B(E2)$ values a spectrum with 1000 counts is generated, comparable to the level of statistics in the experimental spectrum. The simulation does not include background components as it generates the pure FEP delayed coincidence time-difference spectrum. It aims to reproduce only particular features of the FEP spectrum that are accessible for extraction from the experimental spectrum. Those include the normalized areas $\alpha$ and $\beta$ of the two parts of the partitioned distribution below and above the partitioning point $T_p^D = 2$ ns, respectively. In addition, the value $\tau_{\mathrm{exp}} = 313(23)$ ps, deduced after applying the background correction procedure, is equal to the centroid $C_\alpha$ of the part of the delayed distribution with $\Delta T < 2$ ns. These three parameters, $C_\alpha, \alpha$ and $\beta$, are the only experimentally accessible features of the partitioned time-difference distribution, and they are not independent, as shown in the Appendix.

The experimental values $\alpha_{\mathrm{exp}}$ and $\beta_{\mathrm{exp}}$ can be determined from the total number of FEP coincidence counts in the experimental spectra below and above the $T_p^D$ point, respectively. From the total area of the delayed time-difference spectrum in Fig. 5(c) and the measured $p/b$ ratios, approximately 600 FEP coincidence counts were determined for the region $\Delta T < 2$ ns. To obtain the number of FEP counts beyond the partitioning point $T_p^D$ the experimental data were sorted without a coincidence window condition between the LaBr detectors. The emerging counts beyond $T_p^D = 2$ ns from the delayed time-difference distribution contain both FEP and random-background coincidences. For the antidelayed distribution, however, only random-background coincidences are expected at time differences $\Delta T > 2$ ns. The pure FEP counts in the region $\Delta T > 2$ ns can then be assessed by constructing cumulative distributions for the delayed and antidelayed time-difference spectra. This procedure is carried out for both positive ($\Delta T > 2$ ns) and negative ($\Delta T < -2$ ns) time differences, as shown in Fig. 8. An averaged excess of 20(9) FEP counts above the background level is obtained. From the normalized areas the values $\alpha_{\mathrm{exp}} = 0.968$ and $\beta_{\mathrm{exp}} = 0.032$ are determined. The following target function for minimization is implemented in the Monte Carlo simulation:

$$S = k(\beta - \beta_{\mathrm{exp}})^2, \qquad (8)$$

where $k$ is a scaling factor to control round-off errors. For a fixed value of $\beta_{\mathrm{exp}}$ this target function reaches a minimum for a range of pairs of $B(E2)$ values within the used simulation model.

The Monte Carlo simulation of the delayed time-difference spectrum was performed with 1000 iterations for each pair of $B(E2)$ values from the fine grid of $B(E2, 6_1^+ \rightarrow 4_1^+)$ vs $B(E2, J^\pi \rightarrow 6_1^+)$ points, as described above. The parameters $C_\alpha, \alpha$, and $\beta$ of the partitioned distribution from each iteration were averaged and the value of the target function in Eq. (8) was calculated. Only pairs of $B(E2)$ values for which the averaged centroid $C_\alpha$ was within the uncertainty of the experimental value $\tau_{\mathrm{exp}} = 313(23)$ ps were plotted. The resulting $B(E2, 6_1^+ \rightarrow 4_1^+)$ vs $B(E2, J^\pi \rightarrow 6_1^+)$ map is shown in Fig. 9. We designate the point with the highest $B(E2, 6_1^+ \rightarrow 4_1^+)$ value within the minimum as the upper limit for $B(E2, 6_1^+ \rightarrow 4_1^+)$, which corresponds to the lower limit for $\tau(6_1^+)$. The point with the highest $B(E2, 6_1^+ \rightarrow 4_1^+)$ value within the area of
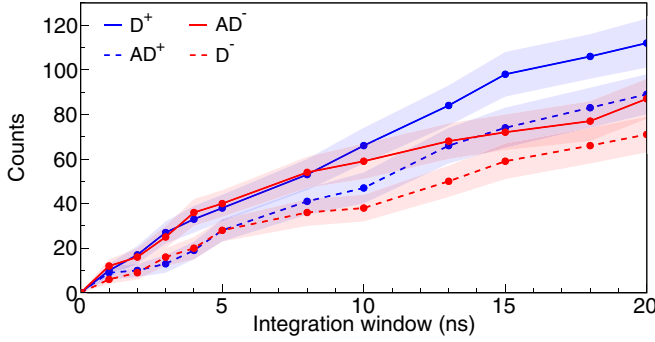
FIG. 8. Cumulative distribution of counts outside the $|\Delta T| = 2$ ns coincidence window for the delayed (D, blue) and antidelayed (AD, red) spectra, constructed starting from the corresponding partitioning points $T_p^{D,AD} = \pm 2$ ns. Positive ($\Delta T > 2$ ns) and negative ($\Delta T < -2$ ns) time differences are denoted by $+$ and $-$, respectively. The $D^+$ and $AD^-$ distributions (solid lines) contain FEP and background counts, while the $AD^+$ and $D^-$ distributions (dashed lines) contain only the respective background counts. The differences $D^+ - AD^+$ and $AD^- - D^-$ provide a measure of the pure FEP counts in the delayed and antidelayed distributions outside the $|\Delta T| = 2$ ns coincidence window, respectively. At integration windows above 10 ns these differences become nearly constant, which indicates that all FEP counts have been accounted for. The average of these two differences, taken at the 20 ns integration window, determines a statistically significant excess of 20(9) FEP counts. Note that the divergence between the $D^+$ and $AD^-$ and the respective $AD^+$ and $D^-$ beyond 8 ns can be interpreted as a change in the underlying distribution of random background coincidences.

the minimum is identified as $(B(E2, 6_1^+ \to 4_1^+), B(E2, J^\pi \to 6_1^+)) = (5.63, 0.12)$ W.u. From this point, we calculate the lower limit for $\tau(6_1^+)$ to be 196 ps. Note that the obtained low value for $B(E2, J^\pi \to 6_1^+) = 0.12$ W.u. indicates an effective lifetime $\tau_{side}$ of the feeding transitions of the order of 1 ns.
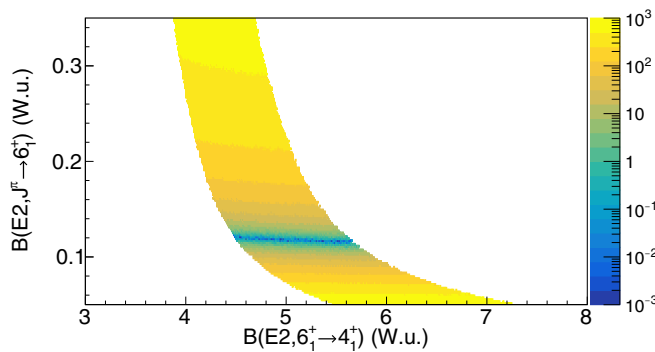


FIG. 9. The averaged value of the Monte Carlo target function [Eq. (8)] for the pairs of $B(E2)$ values around the identified minimum. The points for which the value of $C_\alpha$ differs from $\tau_{exp} = 313(23)$ ps are omitted. The lower limit for $\tau(6_1^+)$ is taken from the point with the highest $B(E2, 6_1^+ \to 4_1^+)$ within the region of the minimum, constrained by the uncertainty in $\tau_{exp}$. At higher $B(E2, J^\pi \to 6_1^+)$ values the resulting band asymptotically approaches the $B(E2, 6_1^+ \to 4_1^+)$ values that correspond to $\tau_{exp}$.

The upper limit of $\tau(6_1^+)$ can be determined from Eq. (7) in the case of $\tau_{side} \approx 0$ ps when the right hand side of Eq. (7) simplifies to $\tau(6_1^+) - \Delta t_p$. The value of $\Delta t_p$ is extracted from simulations by varying $B(E2, 6_1^+ \to 4_1^+)$ with a fixed very high $B(E2, J^\pi \to 6_1^+)$ value of 1000 W.u. for the side-feeding transitions. All obtained values for $\Delta t_p$ are around 3 ps and are deemed negligible compared to the uncertainty of $\tau_{exp}$. The values of $\beta$ obtained from these simulations are less than 0.002, an order of magnitude lower than the experimentally measured $\beta_{exp} = 0.032$. This leads to the conclusion that the assumption of an entirely negligible $\tau_{side}$ is not plausible, which is also consistent with the low value of $B(E2, J^\pi \to 6_1^+) = 0.12$ W.u. obtained from the determination of the lower limit of $\tau(6_1^+)$. In addition, our simulations indicate that for $B(E2, J^\pi \to 6_1^+) < 6$ W.u. ($\tau_{side} > 15$ ps), the $\Delta t_p$ correction is always smaller than the $(1 - f)\tau_{side}$ term in Eq. (7), which ensures that $\tau(6_1^+) \leqslant \tau_{exp}$ within the uncertainties. Therefore we assign the upper uncertainty limit of $\tau_{exp}$, equal to 336 ps, as the upper limit for $\tau(6_1^+)$.

The final value for the lifetime of the $6_1^+$ state in $^{206}$Po is taken as the average of the values from the two limit cases, which produces $\tau(6_1^+) = 266(70)$ ps, where the uncertainty is taken to cover the two limit values. This lifetime corresponds to a reduced transition probability $B(E2; 6_1^+ \to 4_1^+) = 300_{-63}^{+107} \; e^2 \, \text{fm}^4$ or $4.2_{-0.9}^{+1.5}$ W.u. The results for the $4_1^+$ and the $6_1^+$ states are summarized in Table II.

## IV. DISCUSSION

In even-even nuclei the transition from single-particle seniority-type to quadrupole collective excitations can be examined through several experimental criteria. These are the energy of the first excited $2^+$ state $E_x(2_1^+)$, the absolute transition strength $B(E2; 2_1^+ \to 0_{GS}^+)$, and the ratios $R_{J/2} \equiv E_x(J)/E_x(2_1^+)$ and $B_{J/2} \equiv B(E2; J \to J - 2)/B(E2; 2_1^+ \to 0_{GS}^+)$, where $J = 4_1^+, 6_1^+, 8_1^+$ in the case of $^{206}$Po. The expected values for the ratios $R_{J/2}$ and $B_{J/2}$ for the specific cases of a harmonic oscillator and a rigid rotor are useful as indicators for distinguishing between collective and noncollective regimes. Specifically for the $6_1^+$ state, the collective regime is characterized by a relatively low $E_x(2_1^+)$, $R_{6/2} \geqslant 3$, a relatively large $B(E2; 2_1^+ \to 0_{GS}^+)$, and $B_{6/2} \geqslant 1.57$, while the noncollective regime is characterized by a relatively high $E_x(2_1^+)$, $R_{6/2} < 3$, a relatively low $B(E2; 2_1^+ \to 0_{GS}^+)$, and $B_{6/2} < 1.57$ [6,29].

However, the behavior of these observables in the Po isotopes with $N \leqslant 126$ cannot be interpreted unambiguously when one examines closely the levels with different spins. At the $N = 126$ shell closure, $^{210}$Po exhibits a typical seniority structure due to the almost pure $\pi(h_{9/2})^2$ configuration of the yrast $2_1^+, 4_1^+, 6_1^+$, and $8_1^+$ states [30]. Removing only two neutrons, in $^{208}$Po the $2_1^+$ state already begins to acquire collectivity as evidenced by the sudden drop in its excitation energy from 1181 keV in $^{210}$Po to 686 keV in $^{208}$Po [Fig. 10(a)]. In contrast, the energy of the $2_1^+$ state does not change significantly with the removal of more neutron pairs down to $^{200}$Po$_{116}$ (see Fig. 1 in Ref. [12]), which is a behavior associated with a seniority-type configuration [2–4].

TABLE II. The energies of the coincidence conditions, the obtained lifetimes, and reduced transition probabilities in $^{206}$Po.

| State | $E_f$ (keV) | $E_d$ (keV) | HPGe gate (keV) | $\alpha$[a] | $\tau$ (ps) | $B(E2)$ ($e^2$ fm$^4$) | $\tau$ (lit.)[b] (ps) | $B(E2)$ (lit.)[b] ($e^2$ fm$^4$) |
|---|---|---|---|---|---|---|---|---|
| $4_1^+$ | 395 | 477 | 701 | 0.0360(5) | 101(8) | $316_{-23}^{+27}$ | 89(7) | 359(28) |
| $6_1^+$ | 79 | 395 | 701 | 0.0579(9) | 266(70) | $300_{-63}^{+107}$ | | |

[a]Total electron conversion coefficients taken from Ref. [28].
[b]Taken from Ref. [13].

The increased absolute transition strength $B(E2; 2_1^+ \rightarrow 0_{GS}^+) = 18_{-10}^{+14}$ W.u. in $^{206}$Po [12] compared to the $B(E2; 2_1^+ \rightarrow 0_{GS}^+) = 1.8(3)$ W.u. in $^{210}$Po [30] suggests that the $2_1^+$ state in $^{206}$Po has a dominantly collective character [12] (see Fig. 11).

For the higher-spin states, excluding the anomaly at $N = 124$, the $R_{4/2}$ values gradually increase towards the vibrational limit ($R_{4/2} = 2$) yet remain consistent with those of single-particle seniority-type excitations [see Fig. 10(b)]. However, recent lifetime measurements of the $4_1^+$ states in $^{204}$Po and $^{206}$Po indicate that these states are of a collective nature and can be deemed as an admixture of the seniority $\nu = 2$ configurations $\pi(h_{9/2})^2$ and $\nu(f_{5/2})^{-2}$ [13].

In contrast, the isomeric $8_1^+$ states in the even-even Po isotopes with $N \leqslant 126$ are known to be single-particle seniority-type excitations, as established by their constant magnetic moment values (see Table II in Ref. [13]). This is interpreted as the $\pi(h_{9/2})^2$ configuration having a dominant contribution in the wave functions of the $8_1^+$ states [31,32]. The known magnetic moments of the $6_1^+$ states in $^{210}$Po [$|5.48(5)| \mu_N$] and $^{208}$Po [$+5.3(6) \mu_N$] are also comparatively constant and, when scaled with spin, coincide with those of

the $8_1^+$ states ($\approx 7.4 \mu_N$). This implies a dominant role for the $\pi(h_{9/2})^2$ configuration in the wave functions of the $6_1^+$ states in $^{210}$Po and $^{208}$Po. In addition, the relevant neutron orbitals for $^{204-210}$Po, $\nu(2f_{5/2})$ and $\nu(3p_{1/2})$, would not have significant contributions to the wave functions of the $6_1^+$ and $8_1^+$ states in these isotopes.

It is expected, therefore, that the magnetic moment of the $6_1^+$ state would remain constant in $^{206}$Po as well which would establish it as a single-particle seniority-type excited state. The identical behavior of the excitation energy of the $6_1^+$ and $8_1^+$ states [Fig. 10(a)] and of the corresponding ratios $R_{6/2}$ and $R_{8/2}$ [Fig. 10(b)], as well as the low values of the $R_{6/2}$, support this hypothesis. Furthermore, the behavior of $B(E2; 6_1^+ \rightarrow 4_1^+)$ as a function of the neutron number is similar to that of $B(E2; 8_1^+ \rightarrow 6_1^+)$ (Fig. 11) which suggests that the nature of the $6_1^+$ states is the same as that of the seniority-type $8_1^+$ states. The other criterion, the ratio $B_{6/2}$, can be calculated from the result obtained in the current paper and the results from Grahn *et al.* [12], and gives a value of $0.21_{-0.11}^{+0.34}$, which is significantly lower than the vibrational limit of $B_{6/2} = 3$.

All of the aforementioned experimental observables corroborate the hypothesis that the $6_1^+$ state in $^{206}$Po is a single-particle seniority-type excitation. This suggests that for
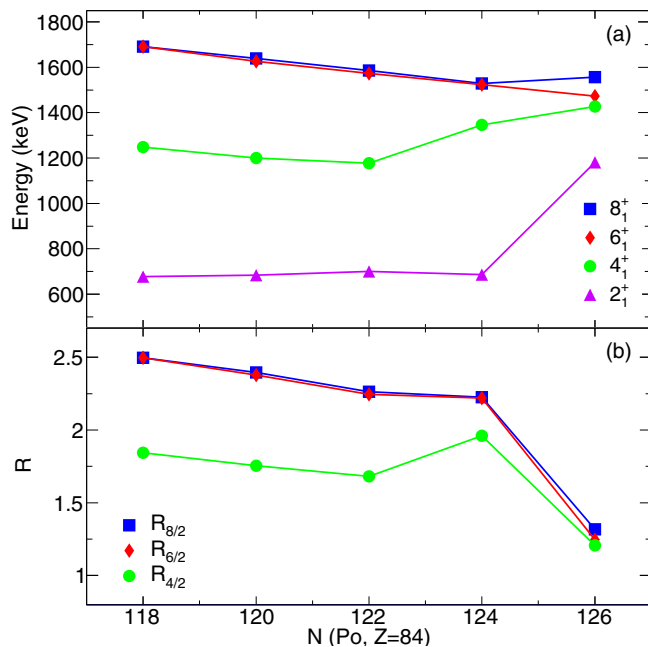


FIG. 10. (a) The evolution of the excitation energy of the yrast states in even-even Po isotopes as a function of the neutron number. (b) The evolution of the $R_{J/2}$ ratios for the $4_1^+$, $6_1^+$, and $8_1^+$ states in even-even Po isotopes as a function of the neutron number.
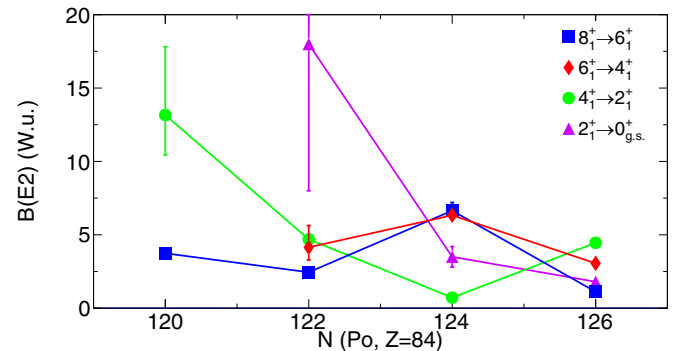


FIG. 11. Experimental $B(E2)$ values for even-even Po isotopes with $N \leqslant 126$. The uncertainty for the $B(E2; 2_1^+ \rightarrow 0_{GS}^+)$ at $N = 122$ is partly omitted to highlight the low-$B(E2)$ region where the systematics of the $6_1^+$ state can be observed. The $B(E2; 6_1^+ \rightarrow 4_1^+)$ values have the same behavior as the $B(E2; 8_1^+ \rightarrow 6_1^+)$ values. Both differ significantly from the behavior of the $B(E2; 4_1^+ \rightarrow 2_1^+)$ values for which collectivity is already present at $N = 122$ [13]. The value for the $6_1^+ \rightarrow 4_1^+$ transition in $^{206}$Po ($N = 122$) is from the current paper. The value for the $4_1^+ \rightarrow 2_1^+$ transition in $^{206}$Po ($N = 122$) is the weighted average between the result from the current paper and that from Ref. [13], while the value for the $4_1^+ \rightarrow 2_1^+$ and $2_1^+ \rightarrow 0_{GS}^+$ transitions in $^{208}$Po ($N = 124$) are taken from Ref. [33].

the $6_1^+$ states in even-even Po nuclei the seniority regime persists down to $N = 122$ and the transition to collectivity occurs at $N \leqslant 120$.

## V. SUMMARY

In the present paper we have confirmed the lifetime of the $4_1^+$ state in $^{206}$Po recently measured in Ref. [13]. Also, we report of the first lifetime measurement using the GCD method on x-ray–$\gamma$ coincidences to determine the previously unknown lifetime of the $6_1^+$ state in $^{206}$Po. Both results contribute to the studies on the spin dependence of the transition from single-particle excitations to collective excitations. The derived absolute transition strength value $B(E2; 6_1^+ \rightarrow 4_1^+)$ and other experimental observables were used to identify the structure of the $6_1^+$ state as a single-particle seniority-type excitation. This result is in agreement with systematics of previous studies on $6_1^+$ states in the $N < 126$ Po isotopes, in which transition to collectivity has been ruled out. Therefore, the transition from single-particle to collective mode for the $6_1^+$ states in even-even Po isotopes with $N < 126$ should be expected at $N \leqslant 120$. To localize this transition, the missing $B(E2)$ values of the yrast states of Po isotopes below $^{210}$Po have to be obtained through an exhaustive set of measurements and further supported by large-scale shell-model calculations.

A novel Monte Carlo-based approach was developed to address the difficulties arising from the complicated feeding pattern of the state of interest. New experimentally observed quantities were utilized, emerging from applying the TAC coincidence window condition that entailed additional corrections to the experimental result. More generally, in the application of the GCD method the centroids of the delayed and antidelayed distributions are routinely determined by integrating the experimental spectra in a finite interval, which also leads to the emergence of such corrections. This effect could be significant in certain cases of expected long lifetimes and should be considered when selecting the integration intervals.

The x-ray–$\gamma$ coincidence technique can serve as a complementary tool to the conventional $\gamma$–$\gamma$ fast timing measurements in nuclei populated via EC decays. This technique can be especially useful in measuring lifetimes of excited states that are difficult to populate in a direct reaction. Similarly, if the states of interest lie beneath an isomeric state that would render them inaccessible for both the recoil-distance Doppler shift method and the $\gamma$-$\gamma$ coincidence GCD method, as it is the case in $^{206}$Po. Still, the applicability of x-ray–$\gamma$ coincidences in future studies is expected to be dependent on the fraction of direct feeding of the state of interest by the decay and the effective lifetime contribution of the populated intermediate excited states. Careful consideration of both experimental conditions and level scheme structure will be necessary for a high-precision measurement to be carried out.

## APPENDIX: PARTITIONED TIME-DIFFERENCE DISTRIBUTION

For any distribution partitioned in two adjacent regions by a partitioning point $T_p$ the following expression is valid:

$$C = \alpha C_\alpha + \beta C_\beta. \tag{A1}$$

Here $C$ is the centroid of the entire distribution, $\alpha$ and $\beta$ are the areas of the regions below and above the partitioning point, and $C_{\alpha,\beta}$ are the corresponding centroids of the partial distributions in the two regions. The normalization condition

$$1 = \alpha + \beta \tag{A2}$$

is imposed on the areas of the two regions.

Considering a delayed time-difference distribution with a prompt Gaussian distribution centered at zero the centroid of the total distribution $C$ is equal to the lifetime $\tau$ of the exponential distribution. If a coincidence window condition is applied, which creates a partitioning point, the quantity accessed via the GCD method coincides with the observable $C_\alpha$. Then Eq. (7) can be expressed in this notation as

$$\tau_{\exp} \equiv C_\alpha = C - \Delta t_p. \tag{A3}$$

Combining Eqs. (A1)–(A3) gives the expression for $\Delta t_p$:

$$\Delta t_p = \beta(C_\beta - C_\alpha). \tag{A4}$$

This term is always positive and also $\Delta t_p \rightarrow 0$ when $\beta \rightarrow 0$, which is the case when $T_p \rightarrow \infty$. The centroid $C_\beta$ is not accessible experimentally due to the presence of random background coincidences. In contrast, the contribution to the centroid $C_\alpha$ from the latter is accounted for via the background correction procedure in the GCD method.

[1] M. G. Mayer, Phys. Rev. **78**, 16 (1950).

[2] A. de Shalit and I. Talmi, *Nuclear Shell Theory* (Academic, New York, 1963).

[3] I. Talmi, Nucl. Phys. A **172**, 1 (1971).

[4] I. Talmi, *Simple Models of Complex Nuclei* (Harwood, Switzerland, 1993).

[5] J. J. Ressler, R. F. Casten, N. V. Zamfir, C. W. Beausang, R. B. Cakirli, H. Ai, H. Amro, M. A. Caprio, A. A. Hecht, A. Heinz, S. D. Langdown, E. A. McCutchan, D. A. Meyer, C. Plettner, P. H. Regan, M. J. S. Sciacchitano, and A. D. Yamamoto, Phys. Rev. C **69**, 034317 (2004); and the references therein.

[6] R. F. Casten, *Nuclear Structure from a Simple Perspective* (Oxford University, New York, 2000).

[7] R. F. Casten, Phys. Lett. B **152**, 145 (1985).

[8] H. Mach, A. Korgul, M. Górska, H. Grawe, I. Matea, M. Stǎnoiu, L. M. Fraile, Y. E. Penionzkevich, F. D. Santos, D. Verney, S. Lukyanov, B. Cederwall, A. Covello, Z. Dlouhý, B. Fogelberg, G. DeFrance, A. Gargano, G. Georgiev, R. Grzywacz, A. F. Lisetskiy, J. Mrazek, F. Nowacki, W. A. PPłóciennik, Z. Podolyák, S. Ray *et al.*, Phys. Rev. C **95**, 014313 (2017).

[9] K. Heyde, J. Jolie, J. Moreau, J. Ryckebusch, M. Waroquier, P. Van Duppen, M. Huyse, and J. L. Wood, Nucl. Phys. A **466**, 189 (1987).

[10] N. J. Stone, At. Data Nucl. Data Tables **90**, 75 (2005).

[11] J. J. Ressler, C. W. Beausang, H. Ai, H. Amro, M. A. Caprio, R. F. Casten, A. A. Hecht, S. D. Langdown, E. A. McCutchan, D. A. Meyer, P. H. Regan, M. J. S. Sciacchitano, A. D. Yamamoto, and N. V. Zamfir, Phys. Rev. C **69**, 034331 (2004).

[12] T. Grahn, J. Pakarinen, L. Jokiniemi, M. Albers, K. Auranen, C. Bauer, C. Bernards, A. Blazhev, P. A. Butler, S. Bönig, A. Damyanova, T. De Coster, H. De Witte, J. Elseviers, L. P. Gaffney, M. Huyse, A. Herzáň, U. Jakobsson, R. Julin, N. Kesteloot, J. Konki, Th. Kröll, L. Lewandowski, M. Thürauf, K. Wrzosek-Lipska, and M. Zielińska, Eur. Phys. J. A **52**, 340 (2016).

[13] M. Stoyanova, G. Rainovski, J. Jolie, N. Pietralla, A. Blazhev, M. Beckers, A. Dewald, M. Djongolov, A. Esmaylzadeh, C. Fransen, L. M. Gerhard, K. A. Gladnishki, S. Herb, P. R. John, V. Karayonchev, J. M. Keatings, R. Kern, L. Knafla, D. Kocheva, L. Kornwebel, T. Kröll *et al.*, Phys. Rev. C **100**, 064304 (2019).

[14] M. J. Martin, Nucl. Data Sheets **108**, 1583 (2007).

[15] A. Linnemann, Ph.D. thesis, Universität zu Köln, 2006.

[16] J.-M. Régis, N. Saed-Samii, M. Rudigier, S. Ansari, M. Dannhoff, A. Esmaylzadeh, C. Fransen, R.-B. Gerst, J. Jolie, V. Karayonchev, C. Müller-Gatermann, and S. Stegemann, Nucl. Instrum. Methods Phys. Res., Sect. A **823**, 72 (2016).

[17] M. Shamsuzzoha Basunia, Nucl. Data Sheets **121**, 561 (2014).

[18] J.-M. Régis, H. Mach, G. S. Simpson, J. Jolie, G. Pascovici, N. Saed-Samii, N. Warr, A. Bruce, J. Degenkolb, L. M. Fraile, C. Fransen, D. G. Ghita, S. Kisyov, U. Koester, A. Korgul, S. Lalkovski, N. Mǎrginean, P. Mutti, B. Olaizola, Z. Podolyak, P. H. Regan, O. J. Roberts, M. Rudigier, L. Stroe, W. Urban, and D. Wilmsen, Nucl. Instrum. Methods Phys. Res., Sect. A **726**, 191 (2013).

[19] J.-M. Régis, M. Rudigier, J. Jolie, A. Blazhev, C. Fransen, G. Pascovici, and N. Warr, Nucl. Instrum. Methods Phys. Res., Sect. A **684**, 36 (2012).

[20] P. H. Richter, Estimating errors in least-squares fitting, The Telecommunications and Data Acquisition Progress Report, Vol. 42–122, pp. 107–137, August 15, 1995, https://ipnpr.jpl. nasa.gov/progress_report/42-122/122E.pdf.

[21] J.-M. Régis, M. Rudigier, J. Jolie, A. Blazhev, C. Fransen, G. Pascovici, and N. Warr, Nucl. Instrum. Methods Phys. Res., Sect. A **763**, 210 (2014).

[22] F. G. Kondev, Nucl. Data Sheets **109**, 1527 (2008).

[23] J.-M. Régis, J. Jolie, N. Saed-Samii, N. Warr, M. Pfeiffer, A. Blanc, M. Jentschel, U. Köster, P. Mutti, T. Soldner, G. S. Simpson, F. Drouet, A. Vancraeyenest, G. de France, E. Clément, O. Stezowski, C. A. Ur, W. Urban, P. H. Regan, Zs. Podolyák *et al.*, Phys. Rev. C **95**, 054319 (2017).

[24] J.-M. Régis, A. Esmaylzadeh, J. Jolie, V. Karayonchev, L. Knafla, U. Köster, Y. H. Kim, and E. Strub, Nucl. Instrum. Methods Phys. Res., Sect. A **955**, 163258 (2020).

[25] J. Chen and B. Singh, Nucl. Data Sheets **177**, 1 (2021).

[26] E. W. A. Lingeman, Phys. Scr. **15**, 205 (1977).

[27] J. C. Hardy, L. C. Carraz, B. Jonson, and P. G. Hansen, Phys. Lett. B **71**, 307 (1977).

[28] T. Kibédi Jr., T. W. Burrows, M. B. Trzhaskovskaya, P. M. Davidson, and C. W. Nestor, Nucl. Instrum. Methods Phys. Res., Sect. A **589**, 202 (2008).

[29] A. Bohr and B. R. Mottelson, *Nuclear Structure* (W. A. Benjamin, Inc., London, 1975), Vol. 2.

[30] D. Kocheva, G. Rainovski, J. Jolie, N. Pietralla, A. Blazhev, A. Astier, R. Altenkirch, S. Ansari, Th. Braunroth, M. L. Cortés, A. Dewald, F. Diel, M. Djongolov, C. Fransen, K. Gladnishki, A. Hennig, V. Karayonchev, J. M. Keatings, E. Kluge, J. Litzinger *et al.*, Eur. Phys. J. A **53**, 175 (2017).

[31] N. Bräuer, A. Goldmann, J. Hadijuana, M. Von Hartrott, K. Nishiyama, D. Quitmann, D. Riegel, W. Zeitz, and H. Schweickert, Nucl. Phys. A **206**, 452 (1973).

[32] O. Häusser, T. K. Alexander, J. R. Beene, E. D. Earle, A. B. McDonald, F. C. Khanna, and I. S. Towner, Nucl. Phys. A **273**, 253 (1976).

[33] D. Kalaydjieva, D. Kocheva, G. Rainovski, V. Karayonchev, J. Jolie, N. Pietralla, M. Beckers, A. Blazhev, A. Dewald, M. Djongolov, A. Esmaylzadeh, C. Fransen, K. A. Gladnishki, A. Goldkuhle, C. Henrich, I. Homm, K. E. Ide, P. R. John, R. Kern, J. Kleemann *et al.*, Phys. Rev. C **104**, 024311 (2021).